

# A Velocity Decomposition Approach for Steady Free-Surface Flow

W.J. Rosemurgy, D.O. Edmund, K.J. Maki & R.F. Beck  
(The University of Michigan, U.S.A.)

## Abstract

In this paper a velocity decomposition method is applied to numerically solve for the steady flow of a viscous fluid over a body with a free surface. In our approach, the velocity vector is decomposed into irrotational and vortical components. A steady, non-linear free-surface boundary-integral method is used to solve for the irrotational and viscous flow away from the body. A field method is used to solve for the total velocity on a domain where the flow is vortical, which is near the body and in the wake. The principle of velocity decomposition is used to write the boundary condition on the outer boundary of the near-body field discretization, and for the body boundary condition in the boundary integral equation. The method is used to solve for the separated flow over a deeply submerged circular cylinder, and a bottom-mounted streamlined body with a free-surface.

## INTRODUCTION

The prediction of calm-water resistance is a fundamental task for ship design. Potential flow and computational fluid dynamics (CFD) methods are two common numerical tools used to approach these problems. CFD is used when all physical aspects of the problem need to be modeled. Although difficult, CFD can capture breaking waves, such as those at the bow and in the ship-generated waves, as well as model the boundary layer and turbulent wake. However, CFD approaches applied to high-Reynolds number applications must approximate the turbulence and use models such as the Reynolds-Averaged Navier-Stokes (RANS)

equations, large eddy simulations, detached eddy simulations, etc. that come with a very high cost in terms of computational time and power. In addition, the numerical grids must be quite dense in order to resolve all meaningful flow features. This can result in grids with cell counts on the order of millions of cells. Furthermore, the steady free-surface solution is often obtained using an unsteady formulation which requires many time steps to reach a steady solution and further increases the computational expense. All of these factors contribute to the large computational expense related to performing CFD calculations.

On the other hand, potential flow methods are more often used to predict gross characteristics of the flow - for example, the far-field wave pattern or the pressure on a body due to the wave field. The potential flow assumption of irrotationality is appropriate in the vast majority of the flow field - anywhere outside of the body boundary layer, wake, and wave breaking regions. The irrotational flow is modeled using a single scalar variable whose gradient is the fluid velocity anywhere in the flow domain. Boundary integral methods used to solve for the potential flow require several orders of magnitude less unknowns and thus need a small fraction of the computational time compared to CFD methods. Fully nonlinear methods, such as those presented by Raven (1996), Janson (1997), Scullen (1998), and Beck (1999) have been shown to predict free-surface flows quite well and have been used widely in marine design. However, potential flow approaches cannot model regions where the flow has rotation or vorticity.

The goal of this research is to find a method that provides the solution in the entire fluid domain of the Navier-Stokes problem, while being

more computationally efficient than existing methods that require full field discretization. The majority of the flow in the fluid domain is irrotational and can be expressed in terms of the gradient of a potential field. Rotational flow will be confined to the boundary layer near the body, the wake region downstream of the body, and turbulent regions associated with breaking waves. For the initial research presented in this paper, we examine only submerged bodies and assume there is no wave breaking; as a result, the rotational flow will be restricted to the boundary layer and wake regions. Future work will study surface piercing bodies and breaking wave problems.

To save computational time, one would like to restrict the viscous flow computations to the small rotational region of the flow and use a fast potential method to solve the flow in the irrotational region. The success of the method depends on finding a potential flow that correctly represents the velocity in the real fluid outside the boundary layer and wake. Conventional potential-flow boundary-integral methods prescribe the kinematic boundary condition on the body surface of no flow through the surface. On the free surface the dynamic and kinematic boundary conditions are applied and there must be appropriate conditions at infinity. We call the solution of the conventional potential flow formulation with a no-penetration condition on the body the *inviscid potential*. Unfortunately, because of the influence of the rotational flow field in the boundary layer and rotational wake, the velocity produced by the inviscid potential does not match that of the Navier-Stokes problem even in regions where the Navier-Stokes velocity is practically irrotational (here the Navier-Stokes problem includes the field equations and the no-slip body boundary condition). For high Reynolds number flows with sufficiently slender bodies, the inviscid potential velocity is a very good approximation to the velocity of the Navier-Stokes problem, and undoubtedly useful for many applications. However, this may not always be the case and we wish to find a general method to provide the solution to the Navier-Stokes problem in the entirety of the flow domain.

The proposed method is developed using the principle of velocity decomposition. The starting point is the statement of the the boundary value problem: the Navier-Stokes problem. The decomposition of the velocity produces the opportunity to solve for a potential field governed by the Laplacian, and the means of solving for the *viscous potential*. The viscous potential flow solution is de-

termined in the usual manner but with a modified body boundary condition. All the other boundary conditions will remain the same and traditional boundary element methods can be used. The new body boundary condition consists of two parts. The inviscid part is identical to the usual Neumann condition of the normal velocity of the potential must equal the normal velocity of the body. The viscous component of the generalized body boundary condition results from conservation of mass principles applied to the boundary layer and wake and is formulated so that the potential flow solution will match the real flow solution in the irrotational flow region. The viscous potential is then used to define the velocities on the outer boundaries of a greatly reduced field discretization of the Navier-Stokes equations. The flow on the field discretization is computed using traditional RANS approximations and methods. An iterative procedure is used in which the first step is to compute an inviscid potential flow solution. This is used to define the outer boundary velocities on the field discretization. Using the rotational flow solution, the viscous component of the body boundary condition for the viscous potential is determined. The improved body boundary condition allows a better viscous potential to be determined, which in turn leads to new outer boundary velocities on the field discretization. The process is repeated until proper convergence is achieved, typically 5 to 10 iterations are used although most of the rotational flow influence on the viscous potential is found in the first 1 or 2 iterations. The final result is a complete description of the entire flow field that satisfies the Navier-Stokes problem.

## BACKGROUND

The idea of decomposing the problem to increase computational efficiency is not unique to the current research. Decomposition methods became popular as computational power grew and researchers hoped to include viscous effects in their inviscid computations. One of the earliest approaches used in airfoil design was a three part method where the potential flow was computed using the exact body, the viscous boundary layer equations were solved with boundary conditions from the potential flow and the potential flow was re-computed using a body with a modified thickness due to the displacement effect of the boundary layer.

Velocity decomposition and domain decomposition have been thoroughly investigated in

the literature and a review of some methods is given here (we note that the literature is broad and that we only review a few papers that are particularly important for our current research). Although very closely related, the two approaches are different. Velocity decomposition, sometimes called functional decomposition, involves splitting the velocity vector into different components and using the proper methods to solve for each. A properly stated velocity decomposition is valid everywhere in the fluid domain and can result in a smoother flow field solution compared to a domain decomposition because it avoids the use of compatibility conditions between the boundaries of the different domains. Domain decomposition splits the fluid region into two or more distinct computational domains or zones. A different approach to solving the fluid equations is used on each domain. Most often an inner domain is placed around the body and the viscous flow equations are solved throughout it while a potential flow model is used on an outer domain. Interaction between the different domains occurs through boundary conditions on the shared boundaries. This is the most visible difference between velocity and domain decompositions. In our opinion, velocity decomposition is a method in which the interaction between the two components occurs on the body-boundary.

Larsson et al. (1990) present the code SHIPFLOW which is based on a three-zone domain decomposition. The boundary layer equations are solved along approximately three-quarters of the body, the RANS equations are solved along the rest of the body and in the wake. A velocity potential is used to compute the flow away from these rotational regions. The non-linear velocity potential solution is computed for the body. Then, the pressure distribution is calculated from the potential flow and the viscous boundary layer equations are solved subject to the potential pressure distribution. Finally, the RANS equations are solved using boundary conditions from the velocity potential and boundary layer solution where possible. This method has been successfully applied to many applications.

In Campana et al. (1995) a two-way coupling procedure is introduced for free-surface ship flows. The RANS equations are solved on an inner domain and a linearized panel method is employed on the outer domain. There is an overlap section where matching conditions are iterated until convergence between the inner and outer solutions is reached.

Iafrati and Campana (2003) study un-

steady wave breaking using the domain decomposition discussed in Campana et al. (1995). In this approach the region of the fluid domain away from the surface is modeled using potential flow and the fluid near the free-surface is solved using the RANS equations with a level-set method.

In Chen and Lee (1996) and Chen and Lee (1999) a technique similar to the method of Campana is introduced except that it employs a non-linear velocity potential formulation. A similar matching technique is applied and the solutions are found to converge within two or three interactions between the viscous and inviscid solutions.

Guillerm and Alessandrini (2003) use a similar approach as Chen and Lee (1999) but employ a free-surface Green function with linearized free-surface conditions to specify the potential velocity in the outer domain. The potential solution is coupled to the RANS solution using a Fourier-Kochin method which allows for the calculation of a potential velocity given a velocity distribution on a boundary. The potential velocity is then calculated and used to supply boundary conditions for the RANS solution. This two-way interaction is repeated until a converged solution is found.

In general, approaches that use domain decomposition suffer from sensitivity in the location of the interface as well as the complexity in specifying the compatibility conditions at the interface between the two domains which, if done incorrectly, can result in irregularities in the velocity and pressure fields.

In a velocity decomposition approach, the velocity vector is generally split into two components. Each component can then be solved for using the most efficient manner with respect to the problem of interest. In Morino (1986), the velocity vector is decomposed into irrotational (curl-free) and solenoidal (divergence-free) components following the Helmholtz decomposition. Morino states the viscous flow equations in a vorticity-based formulation and discusses the differences in the formulation of the boundary conditions for viscous and inviscid flows. Also discussed is the use of a “transpiration velocity”, which was introduced by Lighthill (1958) as an equivalent source method to include viscous effects in an inviscid flow. This is a key element of the present work. Our work is strongly motivated by that of Morino and shares many similarities in formulation. Some important differences are in the way that the vortical velocity is determined. We solve the momentum equations in primitive variables. This is advantageous because we can utilize the wide range of CFD techniques that have been

developed for the momentum equations. Also, the primitive variable solution allows us to develop a unique formulation for the body boundary condition for the viscous potential.

In Hafez et al. (2006) and Hafez et al. (2007) a similar vortical-potential velocity decomposition is used to solve the two-dimensional Navier-Stokes equations. This decomposition is used to derive a Poisson equation from the continuity equation with the vortical component acting as a source term. Pressure is then calculated using a modified Bernoulli equation in terms of the potential solution only. The velocity potential satisfies the inviscid boundary conditions and the viscous terms are solved for using a traditional RANS approach.

The method described in Kendon et al. (2003) also uses a similar irrotational-vortical decomposition but evaluates the inviscid-velocity potential using a frequency-domain approach. The method is applied to problems with wave-body interactions where diffraction forces, which are modeled well by boundary element techniques, have a strong influence on the response. The decomposition is used to modify the Navier-Stokes equations and the modified equations are solved throughout a reduced computational domain. The method is applied to two-dimensional cases and extended to three-dimensions using a strip-theory-type formulation.

Similar to the work done by Kendon and probably the most similar in spirit to the present work is the Spectral Wave Explicit Navier-Stokes equations (SWENSE) method, described in Luquet et al. (2004) and Ferrant et al. (2008). The SWENSE methods uses a highly efficient and accurate velocity potential-based spectral method to model incident waves and then solve a set of modified Navier-Stokes equations to simulate the body motion. Thus all radiation and diffraction effects are represented in the solution on the field discretization. The SWENSE method has been successfully applied to ship maneuvering and wave-body interaction problems. Several advantages of this approach are the extremely accurate formulation for the incident wave field and the fact that the RANS domain does not deform as a result of the body motion.

More recent work on velocity decomposition for a single-phase fluid is found in Kim et al. (2005). Similar to the methods above, the velocity vector is decomposed into an irrotational (expressible by the gradient of a potential) velocity component and a vortical component. The decom-

position is substituted into the RANS equations and, after mathematical manipulation, the “complementary RANS” equations are derived. This new set of governing equations is solved throughout the fluid domain. The method was shown to reproduce the accuracy of traditional RANS simulations but did not exhibit a significant computational speed-up. A reduction in domain size was not realized because the inviscid-velocity potential solution was used and the vortical component was non-zero throughout the majority of the domain. The work of Kim et al. (2005) demonstrated the need to use something other than the inviscid potential, and was important in the development of the current work.

Edmund et al. (2011) uses an irrotational-vortical decomposition to compute the viscous flow over streamlined bodies in an infinite fluid. A viscous-velocity potential is used to represent the irrotational flow and a RANS approach is used for the vortical flow. Motivated by Lighthill (1958) and Morino (1986), a new expression for the body boundary condition for the viscous potential is derived using conservation of mass principles. The new body boundary condition contains an additional term with information about the rotational flow, and is the key advancement to the work done by Kim et al. (2005). The formulation couples the potential and field representations so that the potential sees the rotational flow in the body boundary condition, and the field discretization sees the irrotational flow through the condition on the outer boundary of the reduced domain that encompasses the region where the total velocity has rotation.

In the present paper, the method in Edmund et al. (2011) is extended to include a free-surface. The theory for the velocity decomposition is developed in three-dimensions. To demonstrate the method we have chosen a two-dimensional submerged body as a test problem because it is sufficient to illustrate the benefits of the proposed method. In a real fluid, a free-surface with curvature does have vorticity. At the present stage of development, the viscous-potential satisfies the inviscid free-surface boundary conditions. This is physically justifiable because the vorticity under a free-surface is usually much smaller than that along a wall boundary (at least for the steep but non-breaking waves studied in this paper).

## PRESENT FORMULATION

In this section the governing equations are given and the boundary value problem is stated.

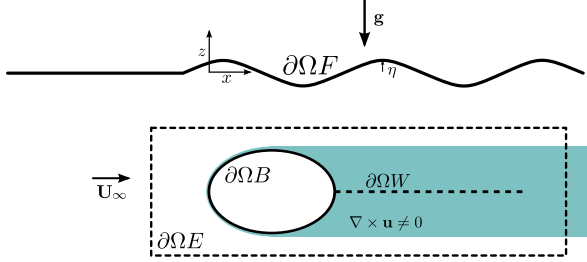


Figure 1: Definition of the boundary value problem showing a fully-submerged body under a free surface.

The velocity decomposition is introduced and its use is described in detail.

### Navier-Stokes Problem

A body fixed, three-dimensional coordinate system is used in this paper. The origin of the coordinate system is located at the intersection of the calm-water plane and the leading edge of the body. As shown in Figure 1, the  $x$ -axis is oriented downstream so that the free-stream velocity,  $\mathbf{U}_\infty = U_\infty \mathbf{i}$ , is positive. The  $z$ -axis is oriented upwards with the gravity vector pointing in the negative  $z$ -direction,  $\mathbf{g} = -g \mathbf{k}$ , and the  $y$ -axis is oriented to starboard in accordance with the right-hand rule.

For problems of interest in this paper the flow is assumed to be adequately described by solutions to the steady incompressible RANS equations:

$$\nabla \cdot \mathbf{u} = 0 \quad (1)$$

$$\nabla \cdot \mathbf{u}\mathbf{u} = -\nabla p/\rho + \nabla \cdot [(\nu + \nu_t)(\nabla \mathbf{u} + \nabla \mathbf{u}^T)] \quad (2)$$

where  $\mathbf{u}$  is the time-averaged fluid velocity vector,  $p$  is the dynamic pressure,  $\rho$  is the density of the fluid,  $\nu$  is the kinematic viscosity, and  $\nu_t$  is the eddy viscosity. The eddy viscosity is an approximation which is used to model the turbulent Reynolds stresses that result from the time averaging of the divergence term in the Navier-Stokes equations. The dynamic pressure is related to the total pressure  $P$  in the relation  $P = p + \rho \mathbf{g} \cdot \mathbf{x}$ . The unknowns  $\mathbf{u}$  and  $p$  are to be determined on the total fluid domain  $\Omega$  that extends between  $\pm\infty$  in the streamwise direction, and between the free-surface and a bottom, if one is present.

The fluid on the body satisfies the traditional no-slip boundary condition requiring the fluid velocity to be equal to the velocity of the body as given in Equation 3.

$$\mathbf{u} = 0 \text{ on } \partial\Omega_B \quad (3)$$

Where  $\partial\Omega_B$  is the surface of the body as shown in Figure 1. Also shown in this figure are the free surface,  $\partial\Omega_F$ , and a wake surface,  $\partial\Omega_W$ , which are used in the potential flow formulation. Finally, we show a portion of the total domain that contains the region over which the total velocity has rotation, called  $\Omega_E$ . The outer boundary of this sub-domain is called  $\partial\Omega_E$ .

The solution must also satisfy the viscous free-surface conditions (that is we neglect the air) on  $\partial\Omega_F$ :

$$\frac{\partial \eta}{\partial t} + \mathbf{u} \cdot \nabla(z - \eta) = 0 \quad (4)$$

$$\bar{\tau} \cdot \mathbf{n} = 0 \quad (5)$$

where  $\eta$  is the free-surface elevation and the stress tensor is  $\bar{\tau} = -P\bar{I} + [\rho(\nu + \nu_t)(\nabla \mathbf{u} + \nabla \mathbf{u}^T)]$ .

Additionally, the flow in the far-field returns to the free-stream velocity vector, satisfying the radiation condition.

$$\lim_{\mathbf{x} \cdot \mathbf{i} \rightarrow -\infty} \mathbf{u} = U_\infty \mathbf{i} \quad (6)$$

We define the governing equations 1 and 2 together with boundary conditions 3 – 6 as the Navier-Stokes problem.

### Velocity Decomposition

A boundary-integral equation (BIE) has the property that the solution in the infinite-free space can be obtained through the integral over a finite area. Another important property of BIE's is that the spatial dimensionality of the problem is reduced by one order. These ideas at least partially explain why numerical methods based on BIE's can be efficient when compared to methods that employ a field discretization of the governing equations. We seek a velocity decomposition that provides a potential field that satisfies the Navier-Stokes problem in the region of space where the total velocity has no rotation. This is perceived as an efficient way to describe the solution, and if the pressure variable is needed, the Bernoulli equation is available.

To arrive at a formulation for the viscous potential, we start with the decomposition of the total velocity vector  $\mathbf{u}$  as the sum of the gradient of the viscous potential and a vortical component  $\mathbf{w}$ :

$$\mathbf{u} = \nabla \varphi + \mathbf{w} \quad (7)$$

Because the definition of the potential requires the total velocity to be irrotational, the vortical component must be non-zero in the region where the total velocity is rotational (close to the body and

in the wake). While we expect the solution to the Navier-Stokes problem to be unique, we have opened up an infinite number of combinations of potential and vortical velocity fields. We seek the decomposition that delivers a vortical velocity field that vanishes with the vorticity vector. If we find such a decomposition, it is apparent that outside the region where the flow is vortical the total velocity is described completely by the gradient of the viscous potential:

$$\mathbf{u} = \nabla \varphi \quad (8)$$

This opens the possibility to solve the governing equations (1-2) on a field discretization that must only encompass the region where the total velocity has rotation, and use Equation 8 as a Dirichlet condition for the velocity on the outer boundary of this reduced discretization.

The total velocity is solenoidal, and the same is assumed about the gradient of the potential. It is in principle possible to have a non-solenoidal vortical velocity that would balance a non-solenoidal potential velocity, but this extra degree of freedom is not envisaged to provide any advantage in the development of the method. Thus the governing equation of the viscous potential is:

$$\nabla^2 \varphi = 0 \quad (9)$$

Green's 2nd identity is used to obtain a boundary integral equation from the Laplace equation with  $\varphi$  being represented as a source distribution over the boundaries of the domain plus a free-stream component.

$$\varphi = \int_{\partial\Omega_B + \partial\Omega_F + \partial\Omega_W} G\sigma dS + U_\infty x \quad (10)$$

Where  $\sigma$  is the strength of the source and  $G$  is a 2-d or 3-d Green Function. The integral extends over a wake surface  $\partial\Omega_W$  to account for the evolution of the rotational part of the velocity vector downstream of the body.

The viscous velocity potential is different from the inviscid potential. The potential boundary value problem is unique so we need a different body boundary condition. To formulate the generalized body boundary condition we apply the velocity decomposition to the no-slip body boundary condition:

$$\mathbf{u} = 0 \quad \text{on } \partial\Omega_B \quad (11)$$

$$= \mathbf{w} + \nabla \varphi$$

or

$$\nabla \varphi = -\mathbf{w} \quad \text{on } \partial\Omega_B \quad (12)$$

The Neumann condition for the viscous potential is:

$$\frac{\partial \varphi}{\partial n} = -\mathbf{w} \cdot \mathbf{n} \quad \text{on } \partial\Omega_B \quad (13)$$

where  $\mathbf{n}$  is the unit normal vector pointing into the body.

Following Lighthill (1958) and Morino (1986) we use the principle of conservation of mass to obtain an expression for the rotational contribution to the generalized body boundary condition for the viscous potential. The divergence operator and the vortical velocity are then expressed in a local coordinate system consisting of a normal vector  $\mathbf{n}$  and two in-plane tangent vectors,  $\mathbf{t}_1$  and  $\mathbf{t}_2$ :

$$\mathbf{w} = w_n \mathbf{n} + w_{t_1} \mathbf{t}_1 + w_{t_2} \mathbf{t}_2 \quad (14)$$

$$\nabla = \frac{\partial}{\partial n} \mathbf{n} + \frac{\partial}{\partial t_1} \mathbf{t}_1 + \frac{\partial}{\partial t_2} \mathbf{t}_2 \quad (15)$$

If the total velocity is solenoidal and the viscous potential satisfies the Laplace equation the divergence of the vortical velocity must be zero:

$$\frac{\partial w_n}{\partial n} + \frac{\partial w_{t_1}}{\partial t_1} + \frac{\partial w_{t_2}}{\partial t_2} = 0 \quad (16)$$

This equation is then integrated in the normal direction out to a distance  $\delta$ .

$$w_n(0) = \int_0^\delta \left[ \frac{\partial w_{t_1}}{\partial t} + \frac{\partial w_{t_2}}{\partial t_2} \right] dn + w_n(\delta) \quad (17)$$

The result is the expression for the normal component of the vortical velocity at the wall. It is now clear how the vortical velocity is used to find the rotational contribution to the boundary condition on the viscous potential field:

$$\frac{\partial \varphi}{\partial n} = -w_n(0) \quad \text{on } \partial\Omega_B \quad (18)$$

$$= - \int_0^\delta \left[ \frac{\partial w_{t_1}}{\partial t} + \frac{\partial w_{t_2}}{\partial t_2} \right] dn - w_n(\delta) \quad (19)$$

We seek a decomposition in which the vortical velocity vanishes with the vorticity as one moves away from the body (in a lateral direction). This means that for a distance  $\delta$  that lies far enough away from the body such that the vorticity is negligible, the desired decomposition will provide a zero vortical velocity and the boundary condition on the viscous potential will have only the integral term in Equation 19. Our expression of the body boundary condition for the viscous potential is directly motivated by the detailed description found in Appendix C of the paper Morino (1986).

The vortical velocity evolves in the wake downstream of the body. This requires that a

source distribution on a wake surface be used. The strength of the source distribution in the wake is also taken to satisfy Equation 19.

On the free-surface the inviscid free-surface boundary conditions are used. This is a simplification that we have chosen because we are currently interested in only the vorticity generated at the body and its influence on the viscous potential. It is felt that for the cases studied in this work with steep but non-breaking waves the vorticity generated by a free-surface is much smaller than that on the body and it is an acceptable simplification.

The inviscid dynamic condition requires that the pressure is constant on the location of the initially unknown free surface.

$$P = 0 \text{ on } \partial\Omega_F \quad (20)$$

The steady inviscid kinematic free-surface condition states that the free surface moves with the fluid. The kinematic condition is traditionally stated as given in Equation 21.

$$\frac{D}{Dt}(\eta - z) = \mathbf{u} \cdot \nabla(\eta - z) = 0 \text{ on } \partial\Omega_F \quad (21)$$

Alternatively, the kinematic condition can be stated as

$$\mathbf{u} \cdot \nabla P = 0 \text{ on } \partial\Omega_F \quad (22)$$

which requires that the pressure at a point on the free surface remain constant and, from the dynamic condition, equal to zero even as that point moves with the free surface. The iterative approach from Scullen (1998) is used in this work to solve for the nonlinear free-surface potential.

A radiation condition is used to ensure that only downstream waves are found. For the steady forward speed problem investigated in this paper, we assume that the vertical gradient of the viscous potential is zero at some distance sufficiently far upstream.

The governing equation (either 9 or 10) together with the new body boundary condition equation 19 and the free-surface conditions 20 and 22 define the boundary-value problem for the viscous potential.

## SOLUTION STRATEGY

In the previous section the decomposed problem is derived in terms of continuous variables. Due to the complexity of the body geometry and solution itself, a numerical method is proposed to solve the decomposed problem. In this section we describe the sequential manner in which the viscous

potential and field variables are determined first, and an overview of the numerical panel method and finite volume method is given.

### Sequential Algorithm

The solution of the viscous potential through the boundary-integral equation and Navier-Stokes equations on a reduced field discretization are performed in an iterative manner. We denote an approximation to the solution of the decomposed problem after  $i$  iterations using a superscript  $(i)$ . This is also called an outer iteration, because the viscous potential and field discretization sub-problems also use iteration (at multiple levels), which will be called inner iterations.

The high-Reynolds number flows of interest in this work are described by Navier-Stokes fields to which the inviscid potential is a good starting point for the velocity field outside the vortical region. This leads us to start the sequential solution procedure by first calculating the potential. The viscous potential at iteration  $i$  is found by solving the following problem:

$$\begin{aligned} \varphi^{(i)} &= \int_{\partial\Omega_B + \partial\Omega_F + \partial\Omega_W} G\sigma dS + U_\infty x \quad (23) \\ \frac{\partial\varphi^{(i)}}{\partial n} &= - \int_0^\delta \left[ \frac{\partial w_{t_1}}{\partial t} + \frac{\partial w_{t_2}}{\partial t_2} \right]^{(i-1)} dn \\ &= -w_n(0)^{(i-1)} + w_n(\delta)^{(i-1)} \end{aligned} \quad (24)$$

where Equation 24 is satisfied on the body and wake surfaces. Also  $\varphi$  must satisfy the free-surface conditions 20 and 22.

For the first iteration, the right-hand side of the body boundary condition is not known, and it is set to zero. This is then the inviscid body boundary condition. Also note the expression for the viscous potential velocity on the body is converted from an integral in the normal direction to a difference between values of the normal component of the vortical velocity at the wall and a distance  $\delta$  from the wall at the previous iteration. This subtle change is very important in the numerical implementation, because evaluation of the normal component of the vortical velocity is trivial. Also, this expression shows that through iteration, if the viscous potential is sufficient to produce a vortical velocity field that decays with the vorticity as one moves laterally away from the body, then the second term in Equation 24 approaches zero upon convergence.

The next step is to find an approximation to the Navier-Stokes equation on a field discretization that encompasses the region where the flow

has vorticity. The reduced domain is shown in the dashed box in Figure 1. With the approximate viscous potential at iteration  $i$ , the approximation to the total velocity and dynamic pressure (and turbulence quantities) are found by solving the following Navier-Stokes problem

$$\nabla \cdot \mathbf{u}^{(i)} = 0 \quad (25)$$

$$\nabla \cdot \mathbf{u}\mathbf{u}^{(i)} = -\nabla p^{(i)}/\rho + \nabla \cdot [(\nu + \nu_t)(\nabla \mathbf{u} + \nabla \mathbf{u}^T)]^{(i)} \quad (26)$$

subject to the boundary conditions that

$$\mathbf{u}^{(i)} = 0 \quad \text{on } \partial\Omega_B \quad (27)$$

$$\mathbf{u}^{(i)} = \nabla \varphi^{(i)} \quad \text{on } \partial\Omega_E \quad (28)$$

The fixed-value velocity condition (Eq. 28) is applied on the inflow and lateral portions of  $\partial\Omega_E$ . On the downstream portion an outflow-type zero-normal-gradient condition is applied to the total velocity vector.

The solution of the Laplace problem is computed for the viscous potential which is followed by the Navier-Stokes problem on the reduced domain. This is repeated until the change in solution between two successive iterations is sufficiently small. It is now seen how the rotational part of the solution influences the viscous potential along the body boundary, and how the irrotational (but viscous) potential flow influences the solution of the Navier-Stokes on a field discretization along the outer boundary of a reduced domain.

## Numerical Formulation for the Viscous Potential Flow

The velocity potential is represented as a distribution of panels over the body and wake surface, and desingularized sources above the free surface. The unknown strengths of the panels and sources are determined through the solution of a linear system of equations that are generated though application of the body and free-surface boundary conditions at a number of collocation points. The number of collocation points on the body and free-surface is equal to the number of body panels and free-surface sources.

For the points on the body and wake surfaces, the source strengths are found by writing an equation that the normal derivative of the viscous potential satisfy Equation 24.

For the collocation points along the numerically predicted free-surface elevation, the free-surface boundary conditions are written as a combination of Equations 20 and 22. For details the

reader is referred to the appendix of the doctoral thesis of Scullen (Scullen, 1998). The body panel influence on a free-surface collocation point is treated by approximating each panel as a discrete source located at the panel centroid. This approximation is quite accurate for distances between body (and wake) panel and free-surface collocation point that are greater than 5 panel lengths, which is always the case in this work.

The free-surface collocation points are located immediately below the free-surface sources. The locations of the point sources are static through the iterative process. The height of the point sources above the free-surface collocation points has an effect on the conditioning of the linear system. The work in Scullen (1998) recommends placing the point sources at a distance equal to the stagnation height,  $h_s = U_\infty^2/2g$ , which is used in this implementation.

The radiation condition requires that all waves generated by the body flow downstream. In some free-surface methods this is accomplished by using an upstream finite-difference operator to calculate the velocity derivatives on the free surface which automatically satisfies the radiation condition (Dawson, 1977). Others use a shift of the upstream collocation points with respect to the source locations. The approach of Scullen (1998) uses analytic expressions for the velocity derivatives so an additional condition must be included. This is accomplished by requiring that the vertical component of velocity is equal to zero at two points sufficiently far upstream from the body.

$$\varphi_z(x = x_1, z = \eta) = 0 \quad (29)$$

$$\varphi_z(x = x_2, z = \eta) = 0 \quad (30)$$

Where  $x_1$  and  $x_2$  are located far upstream of the body (typically a distance of 3 fundamental wavelengths). The distance between the two points must not be equal to an integer multiple of half of the fundamental wavelength because this would allow waves to exist upstream with nodes located at the two points.

$$|x_1 - x_2| \neq n \frac{\lambda_0}{2} \quad (31)$$

Where  $n$  is an integer and  $\lambda_0 = 2\pi U_\infty^2/g$  is the fundamental wavelength.

An iterative procedure, developed by Scullen (1998), is formed by expanding the free-surface conditions about a known free surface and then expressing the potential as the sum of a known component and a perturbation. Note that this iteration is not the outer iteration between the viscous

potential and field discretization, but an inner iteration completely within the viscous-potential subproblem. A combined kinematic-dynamic condition which is linear in the perturbation potential is solved at each iteration. The free-surface elevation is updated using the dynamic condition.

In highly nonlinear problems underrelaxation of the free-surface source strengths is often used in order to increase the stability of the iterative process. Unfortunately, using underrelaxation destroys the quadratic convergence of the method which was observed by Scullen (1998). However, the iterative procedure still converges within a reasonable number of iterations, usually 10 to 15 but up to 25 for the most nonlinear cases.

LAPACK (Anderson et al., 1999) is used to solve the system of linear equations at each iteration. The system is solved using a direct method because the matrix is generally not sparsely populated nor diagonally dominant. The direct method uses an LU-decomposition with partial pivoting to compute a solution. Systems with up to 2,000 unknowns are solved in this research using LAPACK in approximately the same time that is required to compute the influence matrix.

Convergence of the nonlinear viscous potential method is determined by monitoring two quantities. At the end of each inner iteration the  $L_\infty$ -norm (the maximum of the absolute value) of the kinematic condition and dynamic condition are calculated and evaluated as shown in Equations 32 and 33.

$$\max(|p|) \leq \epsilon_1 \cdot g(\eta_{\max} - \eta_{\min}) \quad (32)$$

$$\max(|Dp/Dt|) \leq \epsilon_2 \cdot g^2/U_\infty^2(\eta_{\max} - \eta_{\min}) \quad (33)$$

$$(34)$$

Where  $\epsilon_1$  and  $\epsilon_2$  are set to  $1E - 08$ .

### **Finite Volume Formulation of Navier-Stokes Equations**

To compute the velocity and dynamic pressure on the field discretization we use the open-source CFD library OpenFOAM® (Weller et al., 1998) which solves the RANS equations using the finite-volume method and operates on arbitrary polyhedral grids. The SIMPLE algorithm is used to iteratively solve the system of equations formed by the segregated momentum equations and pressure Poisson equation. Second order numerical schemes are used to approximate the spatial derivatives in the Navier-Stokes equations.

The single equation Spalart-Allmaras turbulence model (Spalart and Allmaras, 1992) is used

to close the turbulence equations by modeling the eddy viscosity. The Spalart-Allmaras model is a near-wall model which does not require wall functions. This requires that the non-dimensional near wall spacing,  $y^+$ , be less than 1.0 along any no-slip boundary.

Convergence of the solution of the finite-volume method is determined based on the residual of the discrete momentum equations. At a given outer iteration, inner iterations on the finite-volume Navier-Stokes system are performed until the largest residual of the momentum system drops by four orders of magnitude.

## **RESULTS**

In this section we present three sets of results. First, the non-linear velocity potential method is validated. Then, the velocity decomposition is applied to the flow over a circular cylinder in an infinite fluid to demonstrate the robustness of the method by solving for separated flow. Finally, results for the flow over a bottom-mounted bump are presented to demonstrate the performance of the velocity decomposition with free-surface effects.

### **Verification of the 2D Non-linear Free-surface Potential Flow Method**

The uniform flow over a 2-dimensional dipole is used to validate the non-linear free surface solver and also to investigate the convergence properties of the non-linear potential flow iterative scheme. The problem set-up is that proposed and studied in Scullen (1998) with  $U_\infty = 1.0$ ,  $g = 1.0$ , and  $h_D = 1$  where  $h_D$  is the depth of the dipole beneath the free surface. Given these properties, the characteristic wavelength from linear theory is  $\lambda_0 = 2\pi$ . The computational domain ranges from  $-1 \leq x/\lambda \leq 5$ . Scullen (1998) performed a systematic study of this problem and found that the value of  $\mu_D = 0.4$  is the maximum value for the dipole strength for which a converged solution can be computed.

First, the results from the present implementation are compared to the free-surface elevation given in Scullen (1998). In Figure 2 the differences between the free-surface elevations are indistinguishable. The computed steepness of the wave is approximately 0.11 which represents a very steep wave.

Next, the convergence properties of the non-linear potential flow iterative method are examined. Figure 3 shows the evolution of the it-

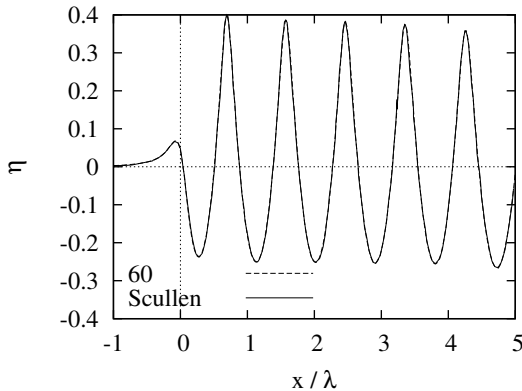


Figure 2: The free-surface elevation resulting from the flow over a dipole under a fully non-linear free surface using 60 sources per wavelength, compared to results from Scullen (1998).

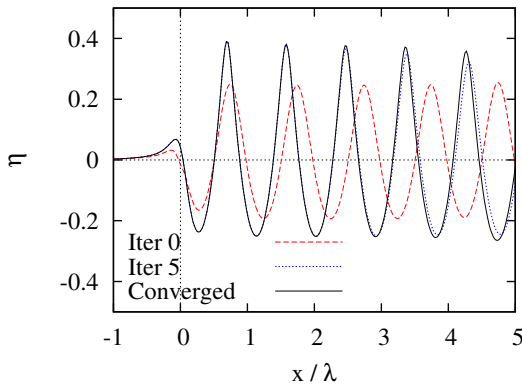


Figure 3: The convergence of the free surface as the iteration procedure progresses.

eration scheme. The nonlinear phenomenon of wavelength shortening is observed. The non-dimensional wavelength of the first iteration is approximately 1.0, or equal to the equivalent linear wavelength. Because this problem is quite nonlinear in nature, underrelaxation of the free-surface source strengths was required. This is why it appears that the wave height grows as the iterations progress. Although the wave height will grow slightly in a case that does not use underrelaxation, the observed drastic growth in this case is mostly due to underrelaxation.

The effect of the density of the sources above the free surface on the convergence of the non-linear potential flow iterative scheme is shown in Figures 4, 5, and 6. Figure 4 shows the converged solution for five distributions of sources ranging from 12 - 60 points per wavelength. It is clear from

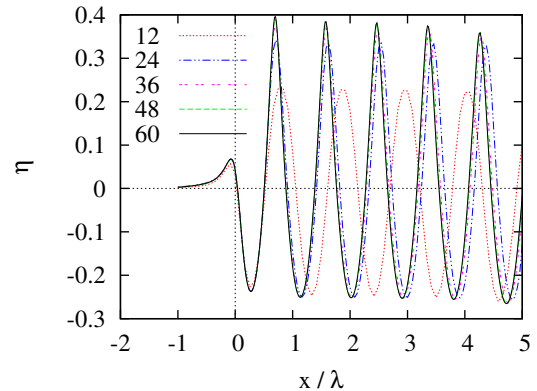


Figure 4: Converged solutions for five different densities of points used to describe the free surface.

the figure that using 12 sources per wavelength is not enough to capture the free-surface in this problem. However, there is little variation in the other converged solutions and the scheme appears to converge as the number of sources is increased.

Figures 5 and 6 show the  $L_\infty$ -norm of the dynamic and kinematic conditions as the iterative scheme converges. All schemes converge to the required tolerances in 12 or fewer iterations however the rate at which they converge varies. Both figures show the same behavior in the iterative scheme - as the number of sources per wavelength grows, the iterative scheme requires more iterations in order to converge. This can be explained by considering the condition of the matrix in the linear system. As the number of sources per wavelength grows, the sources and collocation points become closer together. A single source now has a greater number of collocation points which it has a strong effect on. The result of this is a matrix that has poorer conditioning which in turn results in the denser distributions requiring more iterations to reach convergence. To alleviate this issue, the height of the sources above the free surface should be altered for each given number of sources. Scullen (1998) recommends that the ratio of height to spacing be in the range of 2 - 3. The 24 sources per wavelength has a ratio of 1.9 which agrees with this recommendation.

In summary, the two-dimensional implementation of the non-linear potential flow iterative scheme is shown to converge over a large number of source densities. The difference between the two finest distributions is nearly undetectable. The converged solutions also match with the solution given

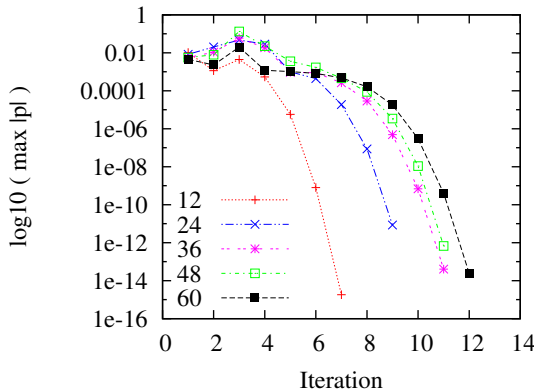


Figure 5: The convergence of the error in the dynamic boundary condition on the free surface.

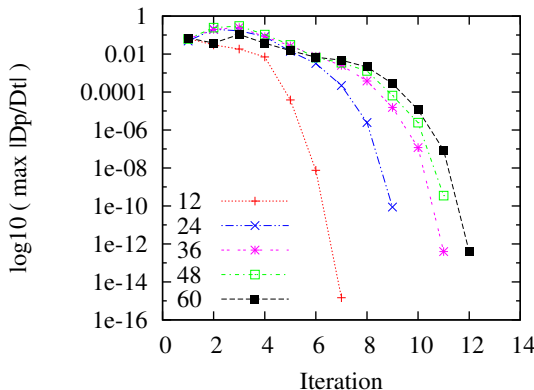


Figure 6: The convergence of the error in the kinematic boundary condition on the free surface.

in Scullen (1998).

### Flow over a Circular Cylinder

To demonstrate the robustness of the velocity decomposition approach, we first present results for the separated flow over a circular cylinder in an infinite fluid. The cylinder has a diameter,  $D$ , of 1.0 m, the free-stream velocity is 1.0 m/s, and  $Re = 320,000$ . Results are presented for two different sized grids using the velocity decomposition. All grids use the same discretization of the body in areas where they overlap. We note that the discretization of the body and fluid domain is relatively coarse with 78 panels representing the cylinder. The relative sizes of the two domains are described in Table 1. Throughout the paper, results shown for the large grid were calculated using a traditional RANS approach (no velocity decomposition) and are used as benchmarks. All results

calculated on smaller domains use the velocity decomposition approach.

Table 1: Discretization details for the Circular Cylinder

Item	Large	Small
Upstream boundary	$75D$	$2D$
Lateral boundary	$75D$	$2D$
Downstream boundary	$60D$	$30D$

Three velocity profiles are presented for this case. The streamwise component of velocity along three different vertical survey lines are shown in Figures 7-9. In these figures, the velocity is made dimensionless with the free-stream value, and the vertical coordinate is made dimensionless with the cylinder diameter  $D$ . All three plots show that the velocity computed with the decomposition converges to that using a conventional RANS technique on the large domain. The solution on the smallest grid compares very well with that on the large grid. Also, we must emphasize that we are only plotting the solution from the decomposition computed on the reduced field domain, but, the solution outside of this region is available through the gradient of the viscous potential.

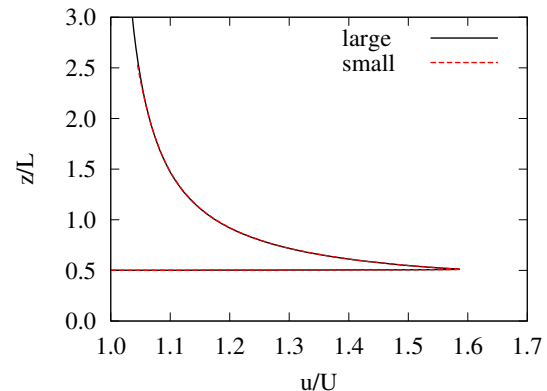


Figure 7: The converged streamwise component of velocity along a vertical survey line beginning at the top of the cylinder using velocity decomposition (small), compared to a RANS solution (large).

### Flow over a Bottom-Mounted Bump

For the purpose of further investigating the velocity decomposition strategy and demonstrating the performance of the solver, the two-dimensional flow over a bottom-mounted bump is

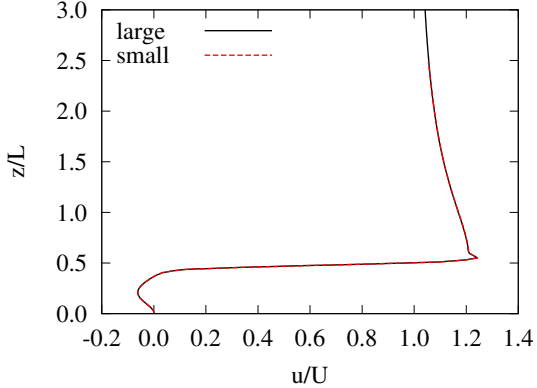


Figure 8: The converged streamwise component of velocity along a vertical survey line beginning at the downstream edge of the cylinder using velocity decomposition (small), compared to a RANS solution (large).

studied. This geometry has been used previously by several authors, including Cahouet (1984), Raven and van Brummelen (1999), and van Brummelen et al. (2000). The geometry of the bump is described by the following equation:

$$z(x) = -1.0 + \frac{27}{4} \frac{H}{L^3} x(x-L)^2, 0 \leq x \leq L \quad (35)$$

where  $H$  and  $L$  are the height and length of the obstacle. To correspond with results from van Brummelen (2002) we use dimensions of  $H = 0.15$  with  $L = 2.0$ . The geometry can be seen in Figure 10. We note that the numerical work of van Brummelen and Raven use a wall boundary condition along the bottom upstream of the body, and the experimentally measured velocity profile as the upstream boundary condition. We do not have the experimental reference in our possession, and since we must assume something about the upstream flow we consider the bottom upstream of the body to be shear-stress free and the flow far-upstream to be uniform.

For both the deeply-submerged and finite-depth cases, the Reynolds number based on body length is  $Re = 3 \times 10^5$ . The finite-depth case is characterized by a water-depth to body-length ratio of 0.5, and a depth-based Froude number of 0.43. The water depth is measured as the calm-water depth. For steady sub-critical finite-depth flows there may be a rise in the free-surface elevation far upstream of the body. This point has been studied in detail by many authors, and the far-upstream dynamic length is sometimes used to describe the water depth.

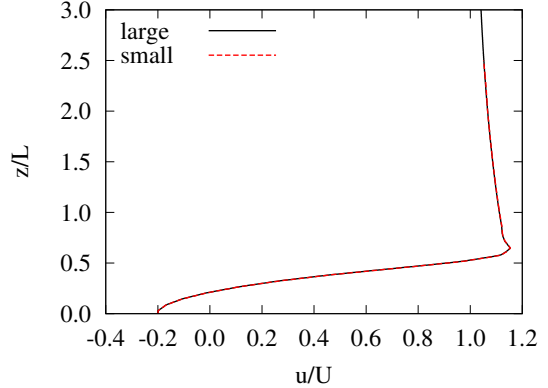


Figure 9: The converged streamwise component of velocity along a vertical survey line beginning one diameter downstream from the trailing edge of the cylinder using velocity decomposition (small), compared to a RANS solution (large).

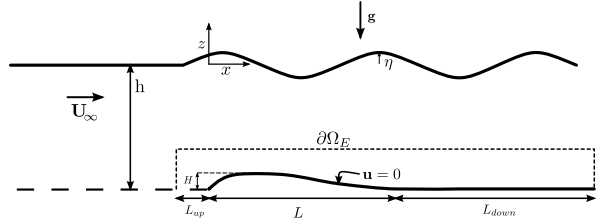


Figure 10: A description of the bottom-mounted bump geometry.

The deeply submerged case is studied with two different sizes of fluid domains, labeled ‘large’ and ‘small’. The dimensions of the large domain extend from 25 body lengths ( $L$ ) upstream from the body, 25 $L$  vertically from the bottom, and 30 $L$  downstream from the body. The small domain extends  $3/8L$  upstream and vertically, and  $12L$  downstream. The relative size of the two domains is shown in Figure 11.

The discretization on the small domain is generated from the large domain. In doing so the discretization is identical in the region almost everywhere that the two regions share in common. Simulations were conducted on three grids for each domain size. The three grid sets are systematically related by a refinement factor of 2, so that each successive refinement generates a grid with four times as many cells. The discretization settings for the finest grids on each domain size are shown in Table 2. All results in the body of the main paper are from calculations on the fine grid; the appendix contains results demonstrating the sensitivity of the

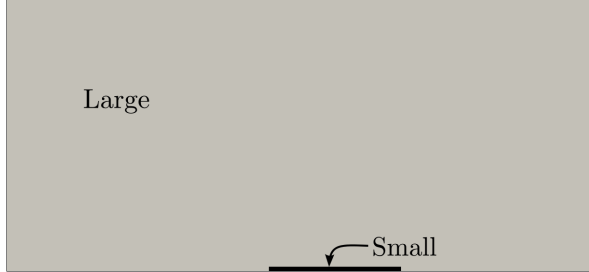


Figure 11: A comparison of the full and reduced domain sizes with the bump - to scale.

Table 2: Discretization for Fine Grid

	variable	large	small
Num. cells in $x$	$N_x$	1,244	888
Num. cells in $z$	$N_z$	392	148
Num. cells on body	$N_L$	400	400
Nearwall spacing	$\Delta z/L \times 10^5$	1.25	1.25

solution to the grid resolution with results from the fine, medium, and coarse grids. The near wall spacing along the body is sufficient for the first grid point to be  $y^+ < 1$  on the coarse grid.

The large grid is used only for the deeply submerged case, and the small grid is used for both the deeply submerged and finite-depth cases.

### Deeply Submerged Case

The main results used to evaluate the performance of the velocity decomposition algorithm are profiles of velocity at three locations along the length of the flow domain. The three sample lines located at  $x/L = 0.5, 1$ , and  $2$  and can be seen in Figure 12. These locations are referred to as midlength, trailing edge, and wake. The colors in this figure are contours of dynamic pressure coefficient ( $C_p = 2p/\rho U^2$ ).

Before the velocity profiles are shown, a contour map of the vorticity field is plotted in Figure 13. In this figure, the contours are shown with a logarithmic scale, and it is seen that the vorticity is contained within a thin layer next to the body in along the wall downstream of the body.

Figures 14-16 show the streamwise component of velocity at the three locations. In each figure the line labeled ‘large’ is the total velocity computed on the large domain using RANS, the remaining four curves show the solution of the potential velocity on the small domain using velocity decomposition. Each of the potential velocity curves is for a different iteration between the RANS

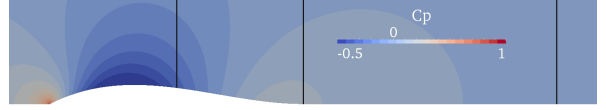


Figure 12: Pressure coefficient and velocity sample lines (midlength, trailing-edge, and wake).

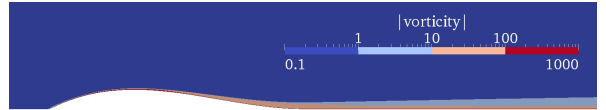


Figure 13: The magnitude of vorticity near the bump in an infinite fluid, calculated on the large domain, logarithmic scale.

and potential flow solution. The zeroth iteration is the inviscid potential velocity, and iterations 1, 2, and 10 are viscous potential results.

In all three figures it is clear that the inviscid potential is a very good approximation to the total velocity. Also, it is shown how the viscous potential in one iteration provides a very accurate solution to the total velocity in the region outside of the boundary layer (the thickness of the boundary layer is about 4% of the body length at the trailing edge).

To ensure that our algorithm allows us to use the viscous potential for the boundary condition on the extent of the small flow domain, we plot the streamwise component of the total velocity for the large domain, and for several iterations on the small domain in Figures 17-19. Again we note that the solution in the infinite domain is known in the decomposed problem, and we only plot the solution on the reduced domain. In these figures it is shown that the final solution on the small domain is very close to that of the final solution on the large domain.

To understand the relationship between the inviscid potential and successive approximations of the viscous potential, the vortical contribution of the generalized body boundary condition for the viscous potential is shown in Figure 20. Here the value of the condition is made dimensionless using the free-stream velocity and is shown for iteration 1, 2 and 10. The value of the boundary condition is relatively small compared to the free-stream magnitude, less than 1%. This is not surprising because the inviscid potential is already a very good approximation for the total velocity for this geometry. The influence of the wall downstream of the body is also visible in this figure.

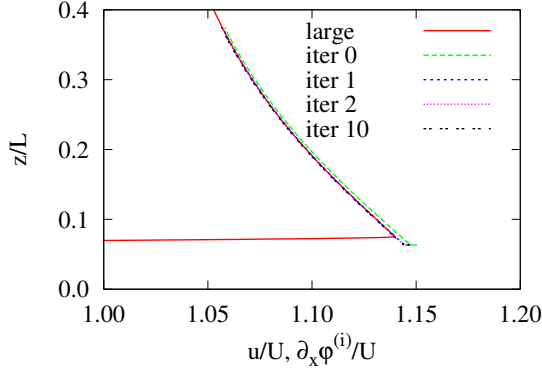


Figure 14: The streamwise potential velocity on the small domain at midlength, compared to the total velocity from the large domain.

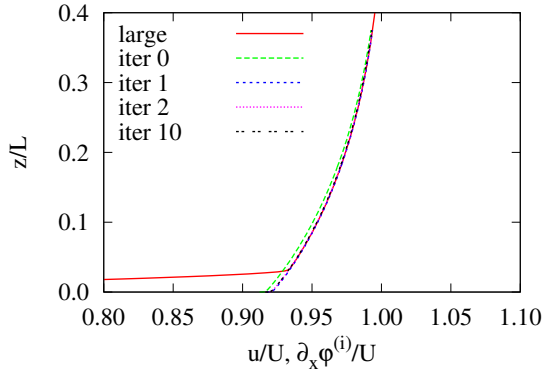


Figure 15: The streamwise potential velocity on the small domain at the trailing edge, compared to the total velocity from the large domain.

### Finite-Depth Case

Next we examine the flow over the bump with a free surface. The depth-based Froude number is 0.43. Figures 21-23 show the streamwise component of the potential velocity compared to the total velocity. All results use the proposed decomposition technique. The first aspect of the results shows how much the free-surface influences the flow over the body. The water depth is one-half the body length, and the fundamental-wavelength-to-body-length ratio is approximately 0.58. Figures 21-23 show that the inviscid potential overpredicts the velocity by about 5% of the total velocity. Also the potential solver converges rapidly and the first iteration between the potential and RANS solvers provides a solution that is very similar to the final solution.

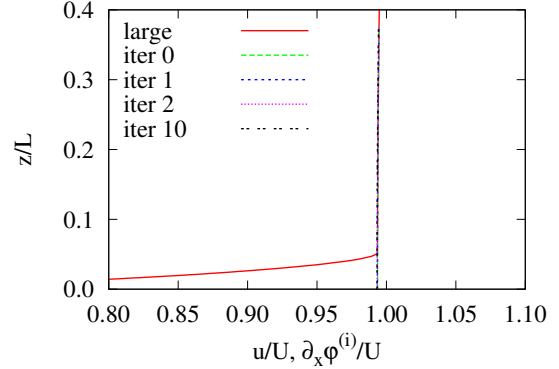


Figure 16: The streamwise potential velocity on the small domain in the wake, compared to the total velocity from the large domain.

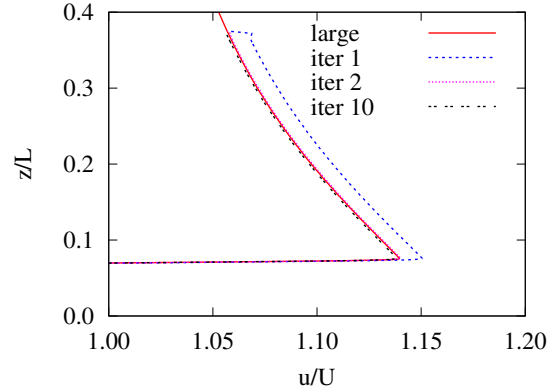


Figure 17: A comparison of velocity, large domain versus small domain at midlength.

The viscous contribution of the generalized body boundary condition for the free-surface viscous potential on the bottom boundary is shown in Figure 24. Comparing this figure to Figure 20 it is seen that the viscous potential velocity is slightly larger than the deeply submerged case. Also, a wave-like behaviour is seen over the portion of the boundary corresponding to the downstream wall.

Finally we examine the free-surface elevation. Figure 26 shows the free-surface elevation predicted with the inviscid potential, and the viscous potential after iteration 1, 2, and 10. The viscous layer on the body is shown to make an important change to the free-surface solution. The viscous free-surface profile shows a rise in the elevation upstream, and a slight shortening and reduction in amplitude of the downstream wave. Also we note that the solution converges rapidly with the profile

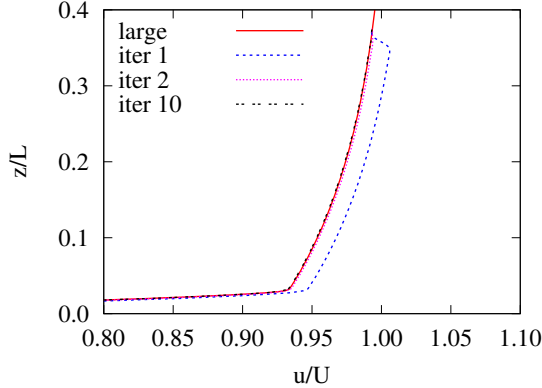


Figure 18: A comparison of velocity, large domain versus small domain at trailing edge.

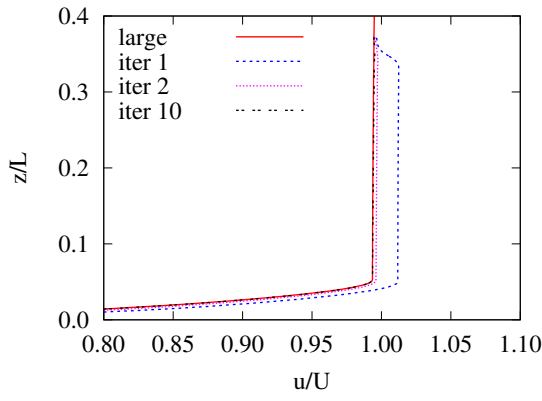


Figure 19: A comparison of velocity, large domain versus small domain in the wake.

for iteration 1, 2, and 10 being practically indistinguishable.

This test case for the finite-depth viscous free-surface flow was studied in detail in the references by van Brummelen (2000, 2002). In Figure 27 we plot our results with those from each of the two references by van Brummelen. We must emphasize that he used the experimentally measured upstream velocity profile and a wall boundary condition on the upstream wall, and this is different than our uniform upstream velocity profile and zero shear stress upstream wall condition. In this figure the free-surface rise upstream of the body is seen to be caused by the viscous flow along the body because it is not observed in the inviscid solution.

## CONCLUSION

In this paper a velocity decomposition approach to solving steady, viscous, free-surface flows

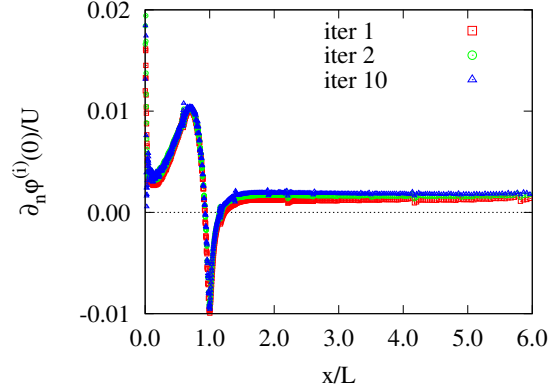


Figure 20: The viscous contribution of the generalized body boundary condition for the viscous potential at three different iterations.

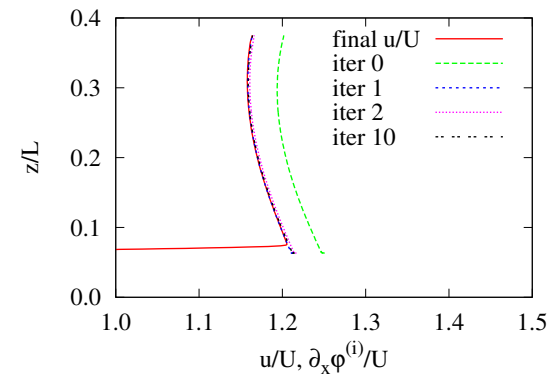


Figure 21: The streamwise potential velocity and final total velocity at midlength for flow over a bottom-mounted bump with a free surface.

is presented. The total velocity vector is decomposed into irrotational and vortical components. A non-linear free-surface velocity potential method is used to calculate a viscous potential that provides the velocity in the region where the total velocity is irrotational. The total velocity and dynamic pressure in the vortical region is found by solving the RANS equations on a reduced domain. The velocity decomposition is applied to the body boundary condition and the external boundaries of the RANS solver. By applying the decomposition to the body boundary condition, an expression is obtained for a generalized body boundary condition that allows for the computation of the viscous velocity potential. The viscous potential is used to supply Dirichlet boundary conditions for the velocity on the outer boundaries of the RANS domain. The improved boundary conditions allow for

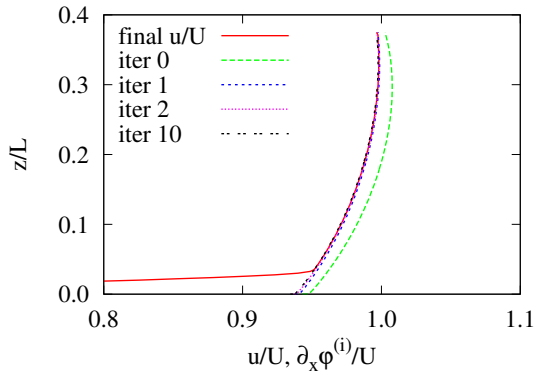


Figure 22: The streamwise potential velocity and final total velocity at the trailing edge for flow over a bottom-mounted bump with a free surface.

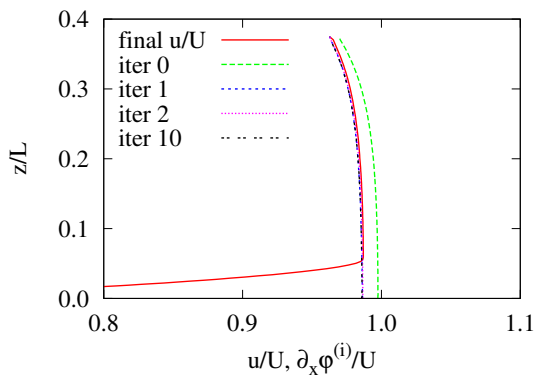


Figure 23: The streamwise potential velocity and final total velocity in the wake for flow over a bottom-mounted bump with a free surface.

the use of reduced computational domains for the RANS solver.

## ACKNOWLEDGEMENTS

This research is supported by the Department of Defense (DoD) through the National Defense Science & Engineering Graduate Fellowship (NDSEG) Program. The authors would also like to gratefully acknowledge the support of a grant from the US Office of Naval Research, Award #N00014-10-1-0301, under the technical direction of Ms. Kelly Cooper as well as the support received through Award #N00014-05-1-0537 under the technical direction of Dr. L. Patrick Purtell.

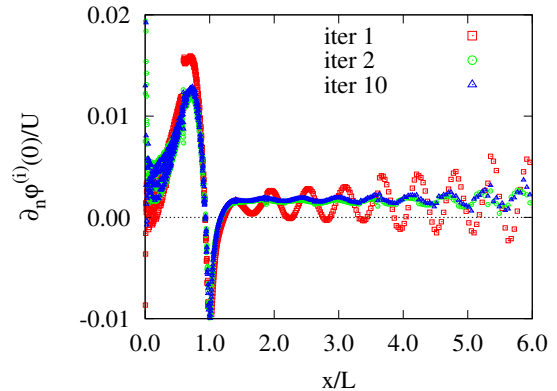


Figure 24: The viscous contribution to the body boundary condition for the viscous potential at three different iterations for the flow over a bottom-mounted bump with a free surface.

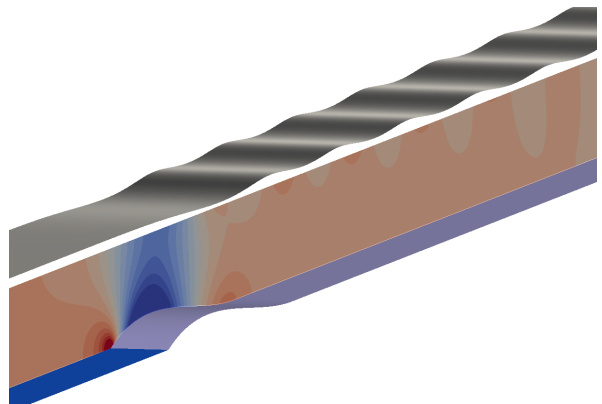


Figure 25: Pressure contours on reduced domain and free-surface elevation.

## References

- Anderson, E., Bai, Z., Bischof, C., Blackford, S., Demmel, J., Dongarra, J., Du Croz, J., Greenbaum, A., Hammarling, S., McKenney, A., and Sorensen, D. *LAPACK Users' Guide*. Society for Industrial and Applied Mathematics, Philadelphia, PA, Third edition, 1999. ISBN 0-89871-447-8 (paperback).
- Beck, R. *Fully nonlinear water wave computations using a desingularized Euler-Lagrange time-domain approach*, chapter 1, pages 1–57. Nonlinear Water Wave Interaction. WIT Press, 1999.
- Cahouet, J. *Etude Numerique et Experimentale du Probleme Bidimensionnel de la Resistance*

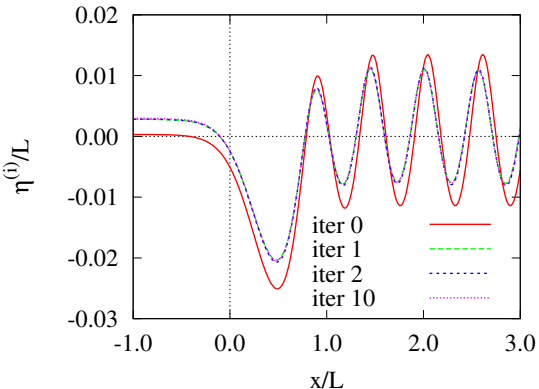


Figure 26: The evolution of the free-surface profile, including viscous effects.

*de Vagues Non-Lineaire*. PhD thesis, ENSTA, Paris, France, 1984.

Campana, E., Di Mascio, A., Esposito, P., and Lalli, F. Viscous-inviscid coupling in free surface ship flows. *International Journal for Numerical Methods in Fluids*, 21(9):699–722, 1995.

Celik, I., Ghia, U., Roache, P., et al. Procedure for estimation and reporting of uncertainty due to discretization in CFD applications. *Journal of Fluids Engineering - Transactions of the ASME*, 130(7), 2008.

Chen, H.-C. and Lee, S.-K. Interactive RANS/Laplace method for nonlinear free surface flows. *Journal of Engineering Mechanics*, 122, 1996. doi: 10.1061/(ASCE)0733-9399(1996)122:2(153).

Chen, H. and Lee, S. RANS/Laplace calculations of nonlinear waves induced by surface-piercing bodies. *Journal of Engineering Mechanics*, 125: 1231, 1999.

Dawson, C. A practical computer method for solving ship-wave problems. In *Proceedings 2nd International Conference on Numerical Ship Hydrodynamics*, pages 30–38. DTIC Document, 1977.

Edmund, D. O., Maki, K. J., and Beck, R. F. An improved viscous / inviscid velocity decomposition method. In *International Workshop on Water Waves and Floating Bodies (IWWFB)*, volume 26, 2011.

Ferrant, P., Gentaz, L., Alessandrini, B., Luquet, R., Monroy, C., Ducrozet, G., Jacquin, E., and

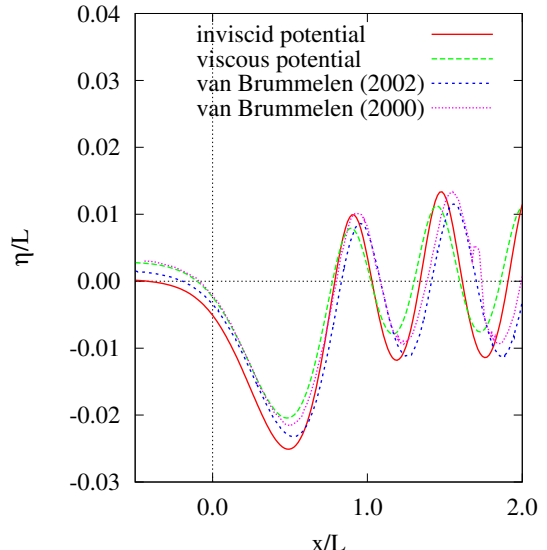


Figure 27: The free-surface profile compared with results of van Brummelen (2000, 2002).

Drouet, A. Fully nonlinear potential / RANSE simulation of wave interaction with ships and marine structures. In *Proceedings of the ASME 27th International Conference on Offshore Mechanics and Artic Engineering*, 2008.

Guillerm, P. and Alessandrini, B. 3D free-surface flow computation using a RANSE/Fourier-Kochin coupling. *International Journal for Numerical Methods in Fluids*, 43(3):301–318, 2003.

Hafez, M., Shatalov, A., and Wahba, E. Numerical simulations of incompressible aerodynamic flows using viscous/inviscid interaction procedures. *Computer Methods in Applied Mechanics and Engineering*, 195(23-24):3110–3127, 2006.

Hafez, M., Shatalov, A., and Nakajima, M. Improved numerical simulations of incompressible flows based on viscous/inviscid interaction procedures. *Computers & Fluids*, 36(10):1588–1591, 2007.

Iafrati, A. and Campana, E. A domain decomposition approach to compute wave breaking (wave-breaking flows). *International Journal for Numerical Methods in Fluids*, 41(4):419–445, 2003.

Janson, C. *Potential flow panel methods for the calculation of free-surface flows with lift*. PhD thesis, Chalmers University of Technology, 1997.

Kendon, T., Sherwin, S., and Graham, J. An irrotational / vortical split-flow approach to vis-

- ous free surface flow. In *2nd MIT Conference on Computational Fluid and Solid Mechanics*, 2003.
- Kim, K., Sirviente, A., and Beck, R. F. The complementary RANS equations for the simulation of viscous flows. *International Journal for Numerical Methods in Fluids*, 48:199–229, January 2005.
- Larsson, L., Broberg, L., Kim, K.-J., and D.-H., Z. A method for resistance and flow prediction in ship design. In *SNAME Transactions*, volume 98, pages 495–535. Society of Naval Architects and Marine Engineers, 1990.
- Lighthill, M. On displacement thickness. *Journal of Fluid Mechanics*, 4(04):383–392, 1958.
- Luquet, R., Gentaz, L., Ferrant, P., and Alessandrini, B. Viscous flow simulation past a ship in waves using the SWENSE approach. In *25th Symposium on Naval Hydrodynamics. St. John's, Newfoundland and Labrador, Canada*, 2004.
- Morino, L. Helmholtz decomposition revisited: vorticity generation and trailing edge condition. *Computational Mechanics*, 1(1):65–90, 1986.
- Raven, H. and van Brummelen, H. A new approach to computing steady free-surface viscous flow problems. In *1st MARNET-CFD Workshop, Barcelona*, 1999.
- Raven, H. *A solution method for the nonlinear ship wave resistance problem*. PhD thesis, TU Delft, 1996.
- Scullen, D. *Accurate Computation of Steady Nonlinear Free-Surface Flows*. PhD thesis, University of Adelaide, February 1998.
- Spalart, P. and Allmaras, S. A one-equation turbulence model for aerodynamic flows. *AIAA Paper*, 92(0439), 1992.
- van Brummelen, E. H., Raven, H., and Koren, B. Numerical solution of steady free-surface Navier-Stokes flow. Technical report, CWI, 2000.
- van Brummelen, H. *Numerical Methods for Steady Viscous Free-Surface Flows*. PhD thesis, University of Amsterdam, 2002.
- Weller, H., Tabor, G., Jasak, H., and Fureby, C. A tensorial approach to computational continuum mechanics using object-oriented techniques. *Computers in physics*, 12:620, 1998.

## APPENDIX - GRID REFINEMENT STUDY

A grid refinement study was performed on the bottom-mounted bump test case using the procedure recommended by the ASME (Celik et al., 2008). Results of the study are given for the bottom-mounted bump in an infinite fluid using the large and small grids described in the body of the paper. A traditional RANS method was used to solve for the flow on the large grid while velocity decomposition was used on the small grid. The two grids were refined twice by doubling the number of cells in the  $x$  and  $z$  directions at each refinement level resulting in coarse (grid 3), medium (grid 2), and fine (grid 1) levels of refinement. To perform the ASME uncertainty analysis, the streamwise component of velocity was sampled at six points. Three locations along the body were chosen,  $x/L = 0.5$ ,  $x/L = 1.0$ , and  $x/L = 2.0$ . At each of those locations, the sample points were located at distances from the body of  $z/L = 0.015$  and  $z/L = 0.25$  corresponding to a location within the boundary layer and a point external to the boundary layer.

Tables 3-6 summarize the results from the uncertainty analysis. In each table, the observed order of accuracy  $p$ , is reported. Also shown are several estimates of the error. The approximate relative error is defined as:

$$e_a^{21} = \left| \frac{\phi_1 - \phi_2}{\phi_1} \right| \quad (36)$$

where  $\phi_i$  is the quantity of interest computed on grid  $i$ . The extrapolated relative error is defined as:

$$e_{\text{ext}}^{21} = \left| \frac{\phi_{\text{ext}}^{12} - \phi_1}{\phi_{\text{ext}}^{12}} \right| \quad (37)$$

where  $\phi_{\text{ext}}^{12}$  is the Richardson extrapolated value of  $\phi$  using the observed order of accuracy. The grid convergence index on the fine grid is defined as:

$$GCI_{\text{fine}}^{21} = \frac{1.25 e_a^{21}}{r_{21}^p - 1} \quad (38)$$

The result of the uncertainty analysis shows that the uncertainty is typically less than 1% and takes a maximum value of 1.49%.

Figures 28-33 show the streamwise component of velocity calculated using RANS and velocity decomposition plotted against a relative refinement factor  $h_i/h_1$  where  $h_i$  represents the average cell size on grid  $i$  and  $h_1 < h_2 < h_3$ . The Richardson extrapolated value is also shown at  $h_i/h_1 = 0$ .

Figures 34-36 show the velocity profiles for the large grid using traditional RANS techniques.

Figures 37-39 show the velocity profiles on the small grid using velocity decomposition.

Table 3: Discretization error and uncertainty at  $z/L = 0.015$  using RANS

	mid length	trailing edge	wake
$p$	0.722	0.689	0.834
$e_a^{21}$	0.0062	0.0032	0.0026
$e_{\text{ext}}^{21}$	0.0094	0.0052	0.0033
$GCI_{\text{fine}}^{21}$	0.0119	0.0065	0.0041

Table 4: Discretization error at  $z/L = 0.015$  using velocity decomposition

	mid length	trailing edge	wake
$p$	0.926	0.876	0.386
$e_a^{21}$	0.0055	0.0027	0.0037
$e_{\text{ext}}^{21}$	0.0060	0.0032	0.0118
$GCI_{\text{fine}}^{21}$	0.0076	0.0040	0.0149

Table 5: Discretization error at  $z/L = 0.25$  using RANS

	mid length	trailing edge	wake
$p$	2.23	3.73	2.15
$e_a^{21}$	0.0000	0.0000	0.0001
$e_{\text{ext}}^{21}$	0.0000	0.0000	0.0000
$GCI_{\text{fine}}^{21}$	0.0000	0.0000	0.0000

Table 6: Discretization error at  $z/L = 0.25$  using velocity decomposition

	mid length	trailing edge	wake
$p$	4.43	2.79	1.51
$e_a^{21}$	0.0001	0.0002	0.0008
$e_{\text{ext}}^{21}$	0.0000	0.0000	0.0004
$GCI_{\text{fine}}^{21}$	0.0000	0.0000	0.0005

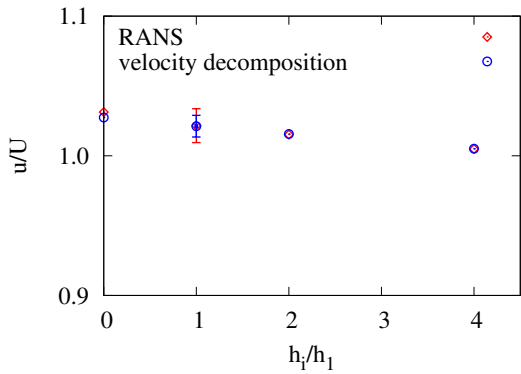


Figure 28: A comparison of the streamwise components of velocity at  $z/L = 0.015$  at the midlength.

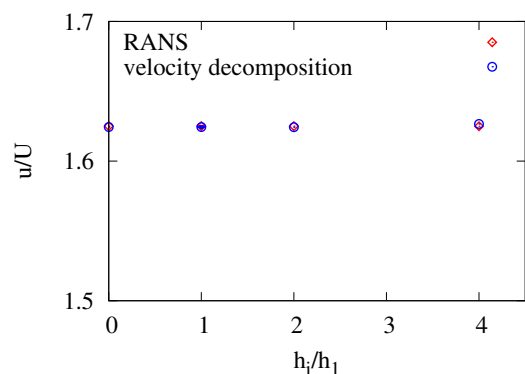


Figure 31: A comparison of the streamwise components of velocity at  $z/L = 0.25$  at the midlength.

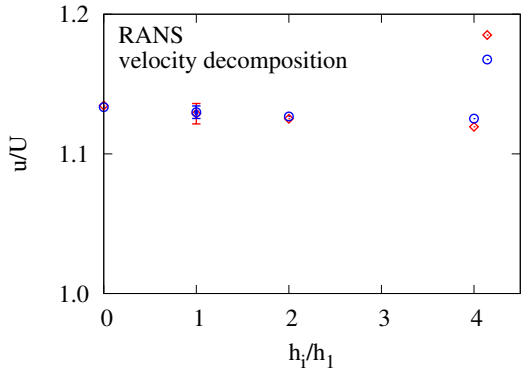


Figure 29: A comparison of the streamwise components of velocity at  $z/L = 0.015$  at the trailing edge.

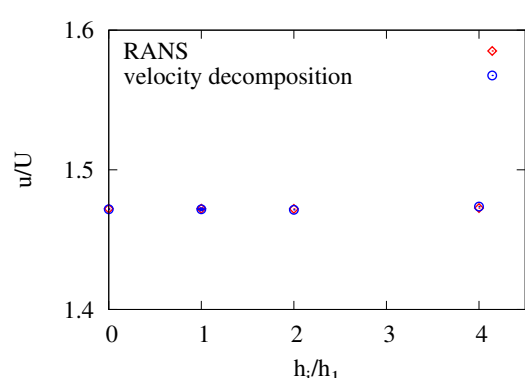


Figure 32: A comparison of the streamwise components of velocity at  $z/L = 0.25$  at the trailing edge.

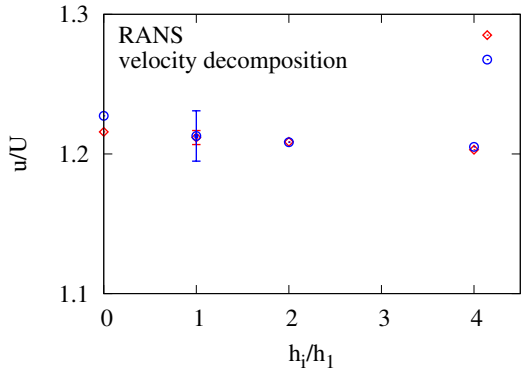


Figure 30: A comparison of the streamwise components of velocity at  $z/L = 0.015$  in the wake.

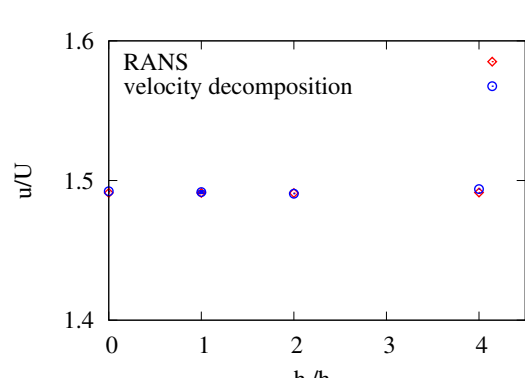


Figure 33: A comparison of the streamwise components of velocity at  $z/L = 0.25$  in the wake.

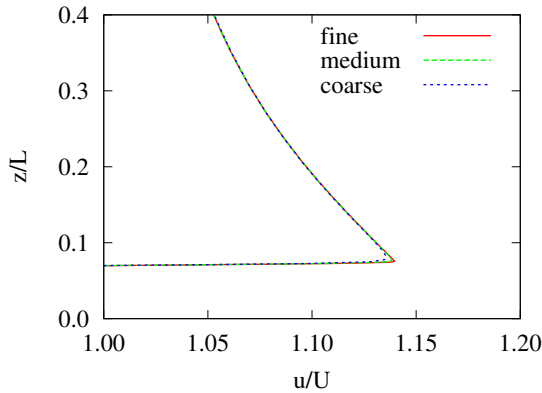


Figure 34: The streamwise component of velocity at the midlength of the body on the large grid.

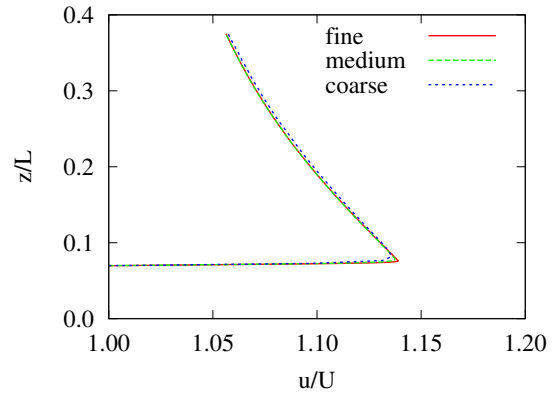


Figure 37: The streamwise component of velocity at the midlength of the body on the small grid using velocity decomposition.

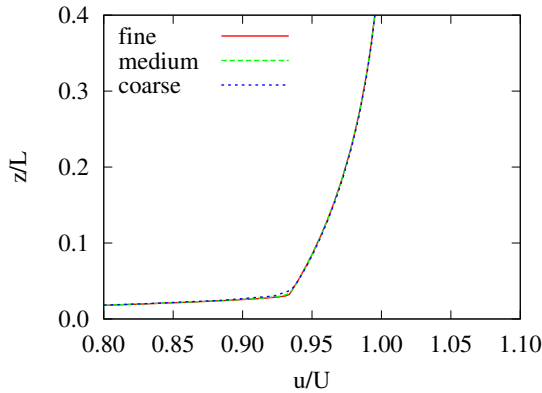


Figure 35: The streamwise component of velocity at the trailing-edge of the body on the large grid.

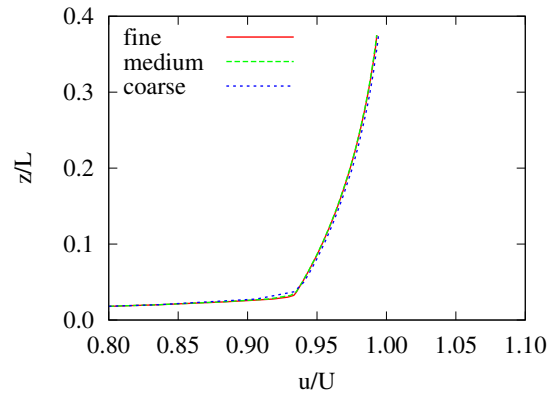


Figure 38: The streamwise component of velocity at the trailing-edge of the body on the small grid using velocity decomposition.

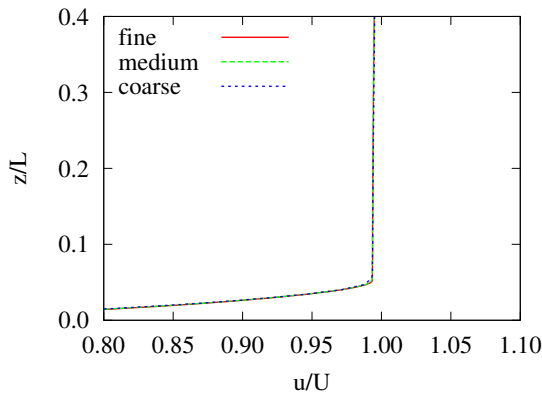


Figure 36: The streamwise component of velocity in the wake on the large grid.

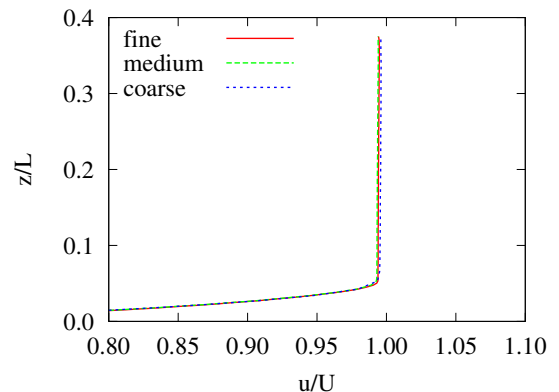


Figure 39: The streamwise component of velocity in the wake on the small grid using velocity decomposition.